Article

Photocatalytic Degradation of Methylene Blue and Metanil Yellow Dyes Using Green Synthesized Zinc Oxide (ZnO) Nanocrystals

S. Shwetha Priyadharshini [1], Jayachamarajapura Pranesh Shubha [2,*], Jaydev Shivalingappa [1], Syed Farooq Adil [3,*], Mufsir Kuniyil [3], Mohammad Rafe Hatshan [3], Baji Shaik [4] and Kiran Kavalli [5]

[1] Department of Chemistry, SJB Institute of Technology, Kengeri, Bangalore 560060, India; shwethapriyadharshini813@gmail.com (S.S.P.); jayadev@sjbit.edu.in (J.S.)
[2] Department of Chemistry, Don Bosco Institute of Technology, Mysore Road, Bangalore 560074, India
[3] Department of Chemistry, College of Science, King Saud University, P.O. Box 2455, Riyadh 11451, Saudi Arabia; mkuniyil@ksu.edu.sa (M.K.); mhatshan@ksu.edu.sa (M.R.H.)
[4] Department of Advanced Materials Engineering for Information and Electronics, Kyung Hee University, 1732 Deogyeong-daero, Giheung-gu, Yongin-si 446-701, Gyeonggi-do, Korea; shaikbaji2@khu.ac.kr
[5] Department of Mechanical and Automobile Engineering, School of Engineering and Technology, CHRIST University, Bangalore 560074, India; kiran.k@christuniversity.in
* Correspondence: shubhapranesh@gmail.com (J.P.S.); sfadil@ksu.edu.sa (S.F.A.)

Abstract: In this work, ZnO nanocrystals (NCs) have been effectively synthesized by a simple, efficient and cost-effective method using coconut husk extract as a novel fuel. The synthesized NCs are characterized by UV-Vis, XRD, FT-IR, SEM, EDX, Raman and PL studies. The obtained ZnO were found to be UV-active with a bandgap of 2.93 eV. The X-ray diffraction pattern confirms the crystallinity of the ZnO with hexagonally structured ZnO with a crystallite size of 48 nm, while the SEM analysis reveals the hexagonal bipyramid morphology. Photocatalytic activities of the synthesized ZnO NCs are used to degrade methylene blue and metanil yellow dyes.

Keywords: ZnO; coconut husk extract; UV light; photocatalysis

1. Introduction

Nanomaterials have emerged as an inevitable part of modern science due to their disparate physical, chemical or biological properties with regard to their bulk composition. Nanomaterials are generally the particles with a particle size in the range of 1–100 nm. The surface activity of nanomaterials, which results in a greater surface to volume ratio, was one of the vital components which holds an important place in materials science research [1]. The applications of nanomaterials were not limited to materials science, but found profound use in medicines [2–4], catalysis [5,6] and optical reactions [7,8]. Amongst the different nanoparticles, metal oxide nanoparticles have attracted considerable attention and have been attentively studied for the past few years due to their potential technological applications in various fields, including diodes [9], detectors [10], solar cells [11,12] and photocatalysis [13].

Zinc oxide (ZnO) nanoparticles are often chosen among the transition metal oxides owing to their diverse properties, such as high thermal and chemical resistance [13], optoelectrical [14], semiconducting [15,16], catalytic [17], antimicrobial [18,19] and antibacterial [20]. Moreover, this n-type semiconductor has a broad bandgap of ~3.37 eV and significant excitation energy of 60 meV. Consequently, ZnO nanoparticles can be termed as a multifunctional material, with their role in optoelectronics [21], photoluminescence [22], dye degradation [23], acoustic devices [24], pharmaceutical and cosmetic applications [25]. In recent times, degradation of dyes in the aquatic ecosystem using semiconducting ZnO nanoparticles as photocatalysts has been explored for the retrieval of water bodies [26]. ZnO nanoparticles with a relatively high surface area and quantum yield display good

photocatalytic activity with respect to the most common photocatalyst, TiO_2. Another study reported by Alanazi and coworkers employed the Gd/N co-doped ZnO for the degradation of MB, which yielded good results [27].

Synthesis of ZnO nanoparticles was well-established through numerous physical and chemical approaches, such as precipitation [28], the sol-gel method [29], solvothermal or hydrothermal [30], electrochemical [31] and microwave methods [32]. Even though these approaches are direct and feasible, several limitations are recognized through these approaches, including adsorption of traces of toxic chemicals on the synthesized nanoparticles. The evolution of nanobiotechnology has urged the design of a green protocol for the synthesis of nanoparticles, especially for biological and medicinal applications [33]. Various green synthetic procedures [21,34] of nanoparticles are being proposed by global researchers, in which plant-based materials are found to be superior in many aspects. Notably, shape-dependent massive synthesis of nanoparticles can be achieved using plant-based material reagents [1]. Moreover, the cost effectiveness, straightforward and environmentally friendly nature of the nanoparticle synthesis through the green approach are other advantages.

Recently, plant extract-based synthesis of ZnO nanoparticles has been in high demand due to the reproducible, biosafe, cost-effective nature. The capability of plant-based biological materials as reagents for the fabrication of nanoparticles is yet to be fully explored. Herein, we describe the eco-friendly novel synthesis of ZnO nanoparticles using a plant-based material, coconut husk extract. Coconut husk is a fibrous wrapping around the coconut fruit and it is currently employed in the production of rope, floor mats and brushes [35]. Coconut husk is a great source of cellulose, lignin, pentosans and polyphenols such as tannin, hydroxybenzoic acid, ferulic acid, syringic acid and vanillic acid [36,37]. A few reports were available for the antimicrobial and antifungal applications of coconut husk extracts against microorganisms, including bacteria [36–38].

2. Experimental Section

2.1. Materials

Analytical grade $Zn(NO_3)_2 \cdot 6H_2O$ (SDFCL, Chennai, India) was used as-received without further purification. A wastewater sample model was prepared by dissolving methylene blue (MB, SDFCL, India) dye and metanil yellow (Sigma Aldrich, Bangalore, India) separately in distilled water (DW). Borosil glass wares were used throughout the study. Aqueous extract of coconut husk powder was prepared by concentrating 250 mL of distilled water solution containing 200 g of powdered coconut husk until the volume reduced to 50 mL. The extract was filtered and used for the preparation of ZnO nanoparticles.

2.2. Synthesis of ZnO Nanocrystals

Coconut husk extract was prepared by boiling 150 g of coconut husk (obtained during de-husking of matured coconut) in 500 mL of distilled water for 2 h at constant stirring, which was filtered and cooled. This extract was employed as fuel for the combustion synthesis, and 0.595 g of $Zn(NO_3)_2 \cdot 6H_2O$ was mixed with 10 mL of as-obtained coconut husk extract at persistent stirring for approximately 20 min. Thereafter, a resultant gel-like sample was obtained and was calcined in the muffle furnace (Utech Model Q-5247, Delhi, India) at 400 °C. After 10 min, a pale-yellow powder was obtained, which was continued in calcination at the same temperature for 3 h.

2.3. Characterization

The as-synthesized ZnO nanocrystals were characterized by XRD (Bruker, Karlsruhe, Germany), UV-vis (Perkin Elmer, Massachusetts, USA), FT-IR (Bruker, Ettlingen, Germany), FE-SEM and TEM (JEOL, Tokyo, Japan). The XRD characterization was carried out using a Bruker diffractometer (Cu Kα (λ = 1.5406 Å) X-ray source). The spectral characterization was carried out using a PerkinElmer UV-Vis spectrometer and a Bruker IFS 66 v/S spectrometer for UV-Vis and FT-IR spectral analysis, respectively. The microscopic analysis, such as SEM, was carried out to understand the surface morphology, and particle size

analysis was carried out by FE-SEM. TEM images were recorded with a transmission electron microscope, JEOL JEM2100 PLUS, operating at a 200 kV accelerating voltage.

2.4. Photocatalytic Efficiency Measurements

For the present test, 100 mL of aqueous solution of MB/MY dye in different concentrations, viz. 5.0, 10.0, 15.0 and 20.0 ppm, was used for photodecomposition processes. The dosage of the as-synthesized photocatalyst, ZnO nanocrystals, was also varied at 5, 10, 15 and 20 mg. The solution was mixed with the photocatalyst and aerated for 100 min, while kept in the dark and under visible and UV irradiation. The kinetics of the degradation was examined periodically by collecting 3 mL of sample solution in 20 min intervals, which was then subjected to centrifugation. From the absorption spectra obtained using UV-Vis spectroscopy, the initial (C_0) and final (C_t) dye concentrations in the system were estimated and the degradation efficacy was calculated utilizing Equation (1):

$$\text{Degradation efficiency} = \frac{C_0 - C_t}{C_0} \times 100 \tag{1}$$

3. Results and Discussion

3.1. Characterization of the ZnO Nanocrystals

ZnO nanocrystals synthesized using coconut husk extract were analyzed qualitatively and quantitatively by different characterization techniques. UV-Visible spectroscopy was employed for the molecular absorption analysis and the obtained spectrum is depicted in Figure 1. Absorbance of the prepared ZnO nanocrystals was measured in a range of 250–800 nm. A peak hike was observed below 400 nm with an absorption maximum at approximately 355 nm, along with an absorption edge from 380 to 420 nm. This indicates that the synthesized material is photolytically active in the UV domain. The bandgap of the prepared photocatalyst was found to be 2.93 eV, which was calculated from the Kulbeka–Munk function. The value of the bandgap was found to be lower than the reported values, which is usually due to the incorporation or doping of ZnO nanoparticles with other material, and hence this decrease in value can be attributed to the <2% of incombustible remnants of the coconut husk extracts on the surface of the ZnO crystals [39].

To understand the crystal structure of the synthesized ZnO nanomaterials, the XRD spectroscopic technique was utilized. The XRD pattern obtained for the synthesized nanomaterial is illustrated in Figure 2. A series of diffraction lines were generated by ZnO nanocrystals, viz. 31.8°, 34.4°, 36.3°, 47.5°, 56.6°, 62.8°, 66.5°, 67.9° and 69.1°, due to the crystal facets of (100), (002), (101), (102), (110), (103), (200), (112) and (201) planes. All these diffractions are attributed to the most stable ZnO hexagonal phase (wurtzite structure) with a space group of *P6₃mc* (a = 3.248 Å and c = 5.215 Å—JCPDS file number 36–1451) [40]. The highest intensity values of (100), (002) and (101) peaks indicated the polycrystalline nature, in which the maximum growth of ZnO nanocrystals occurred in the (101) direction. The mean crystalline size and the lattice spacing of crystals along the (101) facet of synthesized ZnO nanocrystals were calculated using the Debye–Scherrer equation and Bragg's law, which were found to be ~48 and 0.25 nm, respectively.

The FT-IR spectroscopic analysis of synthesized ZnO nanocrystals was carried out in the frequency range of 400–4000 cm^{-1} and the obtained transmittance spectrum is presented in Figure 3. Chemical bonding present in the several organic functional groups and oxides of metals were resonated at different frequencies in the FT-IR spectroscopic analysis. The infrared spectrum of spherical ZnO nanocrystals usually give rise to a peak at 464 cm^{-1}. Conversely, a peak splitting would happen if the shape was anything other than spherical, such as cylindrical or needle-like [41]. A similar pattern was observed with the synthesized ZnO nanocrystals, exhibiting two characteristic stretching vibrations at 440 and 505 cm^{-1}. A less intense broad peak formed between 750 and 1025 cm^{-1} corresponding to the bending and twisting vibrations of $Zn(OH)_2$ [42]. However, the pure ZnO diffraction pattern was obtained from XRD, which confirmed the presence of $Zn(OH)_2$ impurity in an

insignificant ratio. In addition, another broad peak was obtained at 1250–1550 cm^{-1} due to the bending vibrations of the hydroxyl group, possibly from the absorbed moisture content.
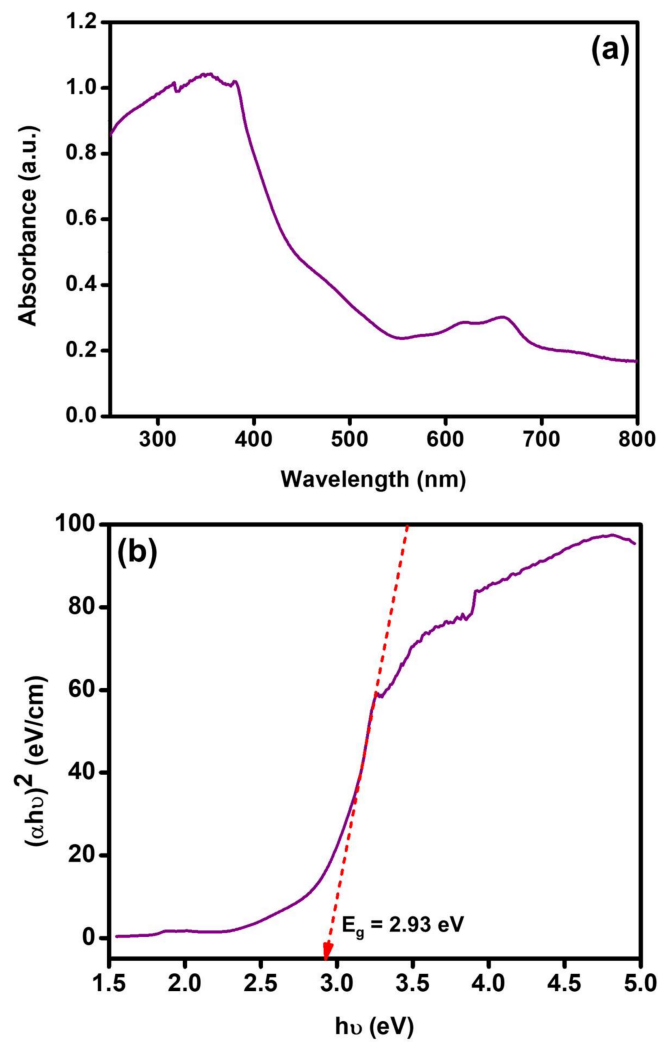

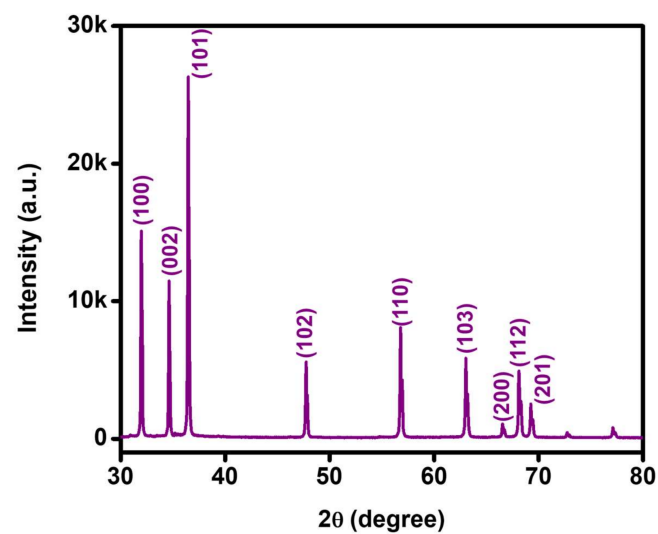**Figure 1.** (**a**) UV-Vis and (**b**) bandgap spectra of the prepared ZnO nanocrystals.

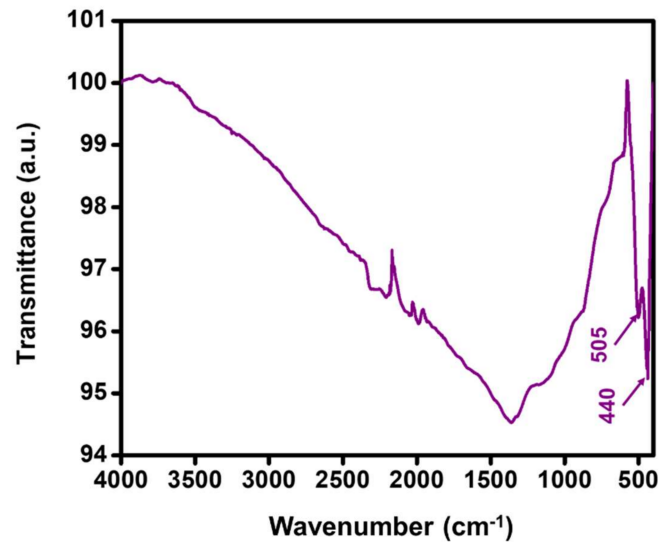**Figure 2.** XRD analysis of the synthesized ZnO nanocrystals.

Figure 3. FT-IR spectrum of the as-prepared ZnO nanocrystals.

The structural characterization of the synthesized ZnO nanocrystals was further carried out by Raman spectroscopic analysis. The attained Raman spectra for the prepared sample are depicted in Figure 4 and are consistent with previous studies [43]. For the wurtzite-like perfect structure, only the optical phonons are involved in first-order Raman scattering at the Γ point of the Brillouin zone, which can be expressed by the following equation:
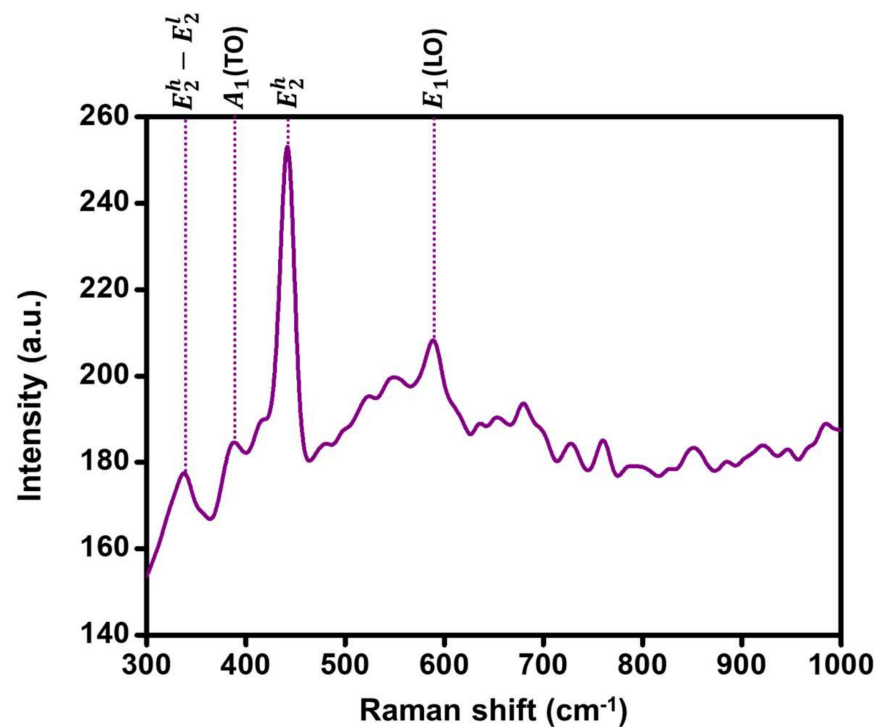
$$\Gamma_{opt} = A_1 + E_1 + 2E_2 + 2B_1 \tag{2}$$

Figure 4. Raman spectrum of the as-prepared ZnO nanocrystals.

Among the different modes represented in Equation (2), only A_1, E_1 and E_2 modes are Raman-active, whereas the B1 modes are Raman-silent. The prominent peak at 440 cm^{-1} was assigned to E_2^h modes, which are non-polar Raman-active modes produced mostly by

oxygen atoms [44]. The stronger E_2 modes and weaker E_1 modes indicate the lower oxygen deficiency in the sample, which in turn proves the good crystal quality [45]. Some other obscure peaks were also noticed in the Raman spectrum of synthesized ZnO nanocrystals at 336, 389 and 589 cm^{-1} assigned to $E_2^h - E_2^l$, A_1(TO) and E_1(LO) modes, where A_1(TO) and E_1(LO) are polar modes [46].

The topographic features of the synthesized ZnO nanocrystals were examined employing FE-SEM. Figure 5a,b represent the two FE-SEM images obtained for the synthesized ZnO nanocrystals in low and high magnifications, respectively. A close observation of the SEM images obtained showed that they are similar to the closely packed hexagonal bipyramid morphology with six facets folded [47]. The two vertical edges of the crystals are slightly distorted. The size of the formed crystals is irregular, as expected upon using the plant extract-based synthetic protocol [48].
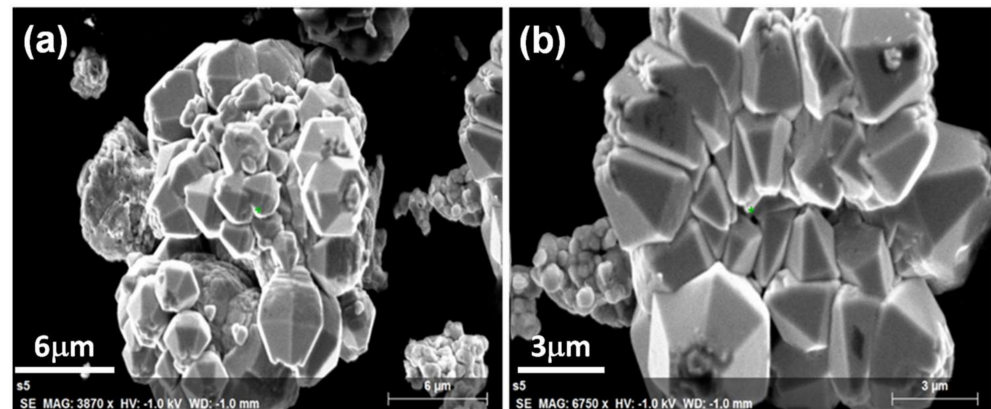

Figure 5. FE-SEM images of the as-synthesized ZnO nanocrystals in (**a**) low and (**b**) high magnification.

The elemental composition of the prepared ZnO nanocrystals was estimated using EDX spectroscopy, and the obtained percentage data are shown in Figure 6. It disclosed that the synthesized heterostructure contained the required elemental composition. Furthermore, the EDX spectra of ZnO nanocrystals revealed that all the predicted elements, such as Zn and O, exist, and the percentage of elemental compositions is shown in the inset table in Figure 6, which is consistent with the desired ZnO.
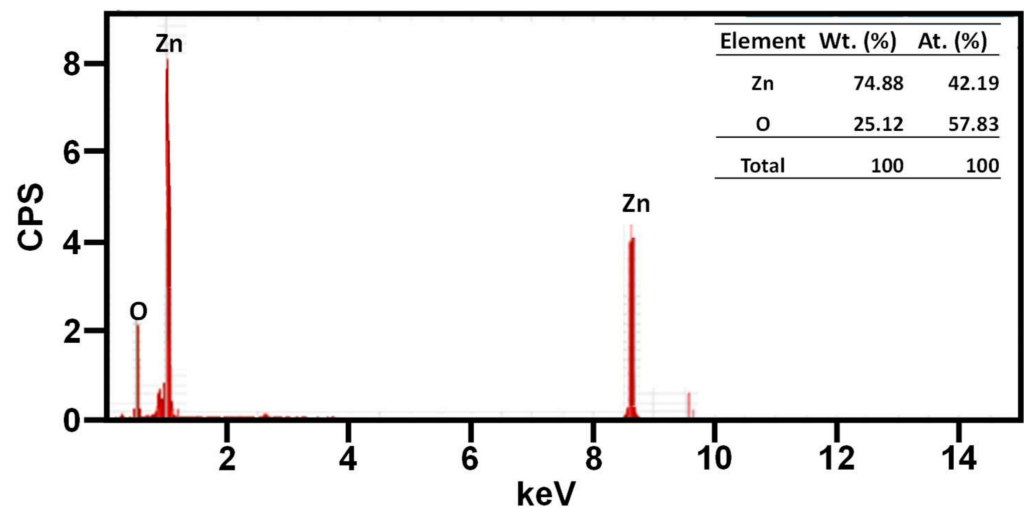

Element	Wt. (%)	At. (%)
Zn	74.88	42.19
O	25.12	57.83
Total	100	100

Figure 6. EDX spectrum of synthesized ZnO nanocrystals.

3.2. Photocatalytic Performance of ZnO Nanocrystals

The important objective of this work is to utilize the synthesized ZnO nanocrystals as photocatalysts for the degradation of methylene blue dyes, a hazardous chemical present in the aqueous emissions from the textile industry. The photocatalytic degradation activity of the synthesized ZnO nanocrystals was studied by varying the different reaction conditions. The theory of semiconductor-based photocatalysis stated that the surface area, bandgap, morphology, crystallinity, particle size and amount of $OH^\bullet$ free radicals on the surface of the photocatalyst determine its photocatalytic efficacy [49]. The theory elucidated the release of electrons and holes on the semiconductor surface by the absorption of light, and the produced electrons and holes will participate in the reaction or reunite. If an additional surface is provided for the electrons and holes before the reunion, they would relocate, where the electrons are caught by the semiconductor while the holes are trapped to produce $OH^\bullet$ and $HO_2^\bullet$. For a ternary structure, more surface is available for relocation of photogenerated charge carriers, and therefore the produced hydroxyl radicals were efficiently utilized to decompose MB dye. As per the results obtained from the UV-Vis spectroscopy, it is obvious that the synthesized nanocrystals are active in the UV domain. Furthermore, the bandgap was calculated to be E_g = 2.93 eV. Parameters such as light source, photocatalyst dose, dye concentration, irradiation time and pH were systematically studied, and MB was selected as the standard pollutant for photocatalytic decomposition in the investigation. The variation of absorption peak intensity recorded at 663 nm (λ_{max} of MB) was monitored to conclude the obtained results.

3.2.1. Influence of Light Source

The photocatalytic decomposition of MB dye in the presence of synthesized ZnO nanocrystals, i.e., 5 ppm MB/MY and 15 mg ZnO, was performed in three different environments, i.e., dark, UV light irradiation and natural solar irradiation. The obtained data are presented in Figure 7. When the degradation experiment was conducted in the dark, the photodegradation of the MB was insignificant. In case of the experiments carried out under visible light irradiation and UV irradiation, the photodecomposition of MB was much higher with UV irradiation. The UV-Vis spectrum of the synthesized ZnO nanocrystals supported the results obtained for the degradation of MB under UV irradiation. In a span of 100 min, ~99% degradation was observed under UV irradiation, whereas 97% degradation of MY was observed. For the corresponding counterpart, i.e., visible light, it brought only ~22% of degradation.
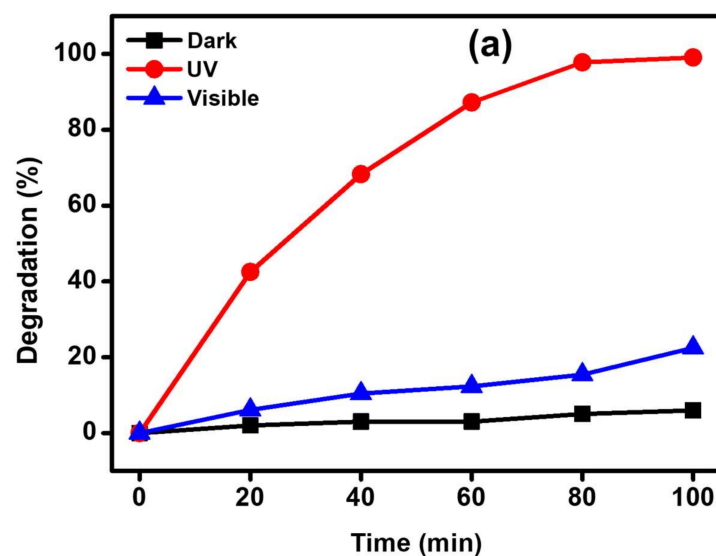

Figure 7. *Cont.*
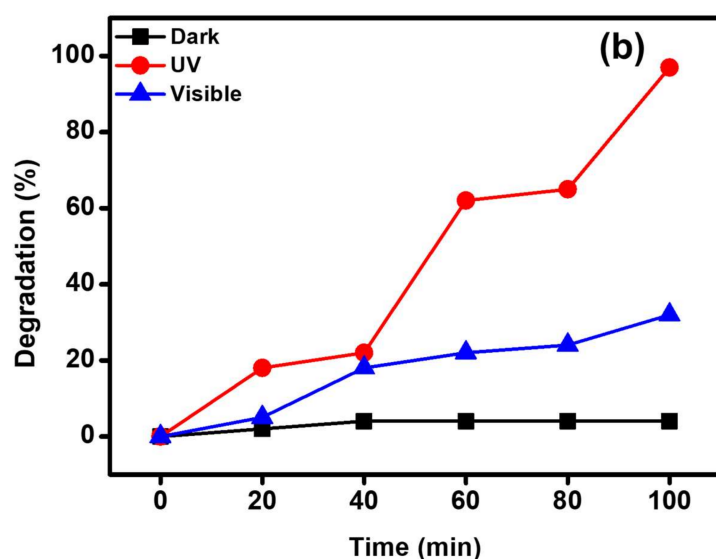
Figure 7. Impact of light source on (**a**) MB and (**b**) MY photodegradation employing the synthesized ZnO photocatalyst.

3.2.2. Influence of the Amount of ZnO Catalyst

After the confirmation of the photocatalyst composition and light source for the efficacious photocatalytic property of the synthesized ZnO nanocrystals, the influence of the photocatalyst dose on the photodegradation of MB/MY was also evaluated by varying the amount of the photocatalyst (5–20 mg) under UV radiation (Figure 8). The results disclosed that the photodecomposition of MB/MY was considerably influenced by the photocatalyst dose. It is apparent that by increasing the photocatalyst dose from 5 to 15 mg, the degradation of MB dye enhanced from ~63% to ~99%, whereas from 61% to 97% for MY. This enhancement in the degradation is directly attributed to the introduction of more photocatalytic active sites in the medium that can generate more radical ions. Nevertheless, a further increase in the photocatalyst dose to 20 mg leads to a decrease in the degradation efficacy to ~88% under the identical photocatalytic conditions, however the degradation of MY was increased to 99% with a photocatalyst dose of 20 mg. When the photocatalyst quantity exceeds a critical boundary, there will not be enough space for the nanocrystals to disperse in the solution and the particles can stick to each other and become aggregated, owing to the particles' surface energy. Hence, most of the photocatalytic active sites were blocked or covered up, and the degradation efficacy of the system decreased [50]. However, when the same reaction was carried out in the absence of the catalyst, it yielded a 9% degradation of MB and 8% for MY under identical conditions. Accordingly, 15 mg was selected as the optimal photocatalyst amount and was utilized for the rest of the experiments to optimize other parameters.

3.2.3. Influence of Concentration of MB/MY

The impact of initial dye concentrations on the decomposition performance of the MB/MY was also assessed by varying the concentration of MB/MY from 5 to 20 ppm under UV irradiation, while maintaining the photocatalyst dose at 15 mg. The attained photocatalytic data are graphically presented in Figure 9a,b. The obtained results disclosed that the photocatalytic performance of the ZnO nanoparticle is inversely proportional to the dye concentration at similar conditions, i.e., maximum degradation efficacy was observed at the lowest MB/MY concentration (5 ppm). By raising the MB concentration from 5 to 20 ppm, the degradation of MB gradually declined from ~99% to ~58% and the degradation of MY was reduced from 97% to 56%. This abatement is owing to the decreased absorption of light on the photocatalyst surface by raising the dye concentration, which in turn reduces the production of OH$^\bullet$ radical ions which play a vital role in the photodegradation process.

Therefore, it is indispensable to keep the ratio of concentration of photocatalysts to dyes alike. Hence, from the obtained results, it can be concluded that the highest degradation performance of the catalyst can be achieved when the MB dye concentration is 5 ppm, while an almost similar degradation was also obtained for the MB dye concentration at 10 ppm. Therefore, it can be said that the photocatalyst can be optimally used for MB and MY dye degradation in the concentration range between 5 and 10 ppm.
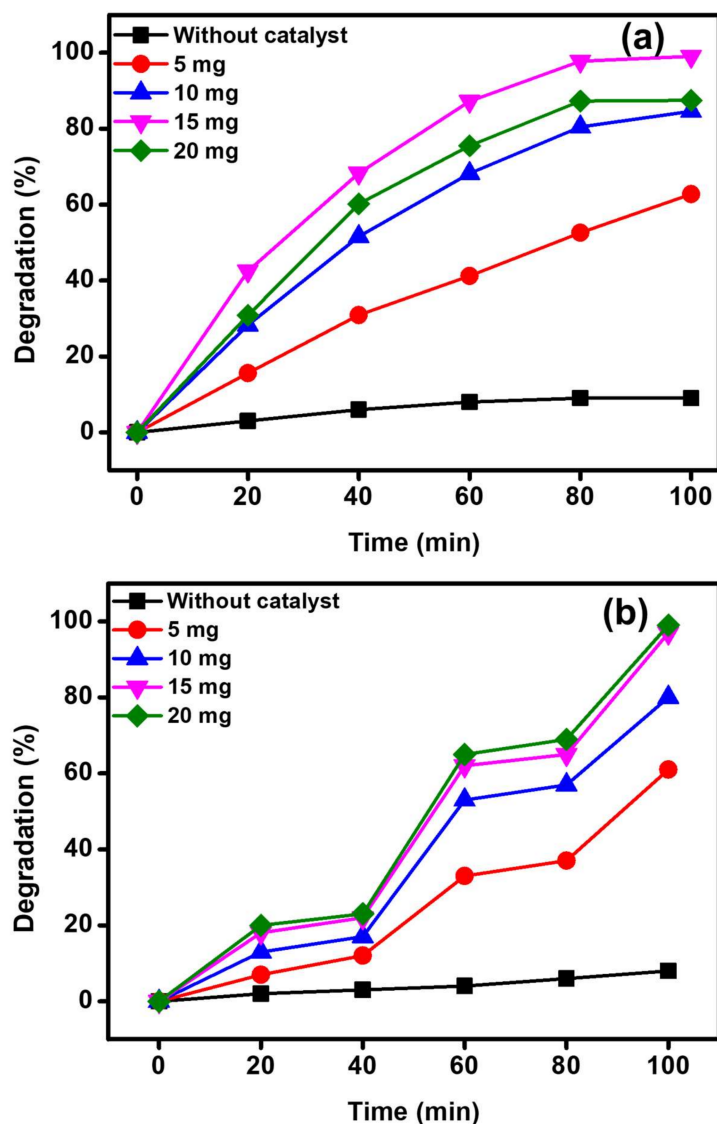

Figure 8. Impact of photocatalyst dose on (**a**) MB and (**b**) MY photodegradation employing the as-synthesized ZnO photocatalyst.

3.2.4. Influence of pH Value

It is well-known that the pH of the solution is one of the most significant parameters in the photocatalytic degradation of organic dyes. This effect is attributed to the change in surface charge of the photocatalyst, which in turn had a considerable effect on the photocatalytic efficacy. Usually, the photocatalytic performance of the photocatalyst is directly related to the availability of OH• radicals in the reaction medium, which improves the photocatalytic decomposition of MB dye by many folds in alkaline aqueous solution. Figure 10 displays the impact of pH value on the photodegradation of MB dye in the presence of the synthesized ZnO photocatalyst. The impact of pH value on the removal of MB/MY was examined at three different pH values of 4, 7 and 10. The results illustrated

that by raising the pH value to 10, higher photodegradation was achieved. At an acidic pH value (i.e., pH 4), the lowest degradation performance was obtained, with ~38% degradation of MB and ~33% degradation of MY. As expected, when the pH of the solution is increased, the ZnO photocatalyst showed maximum degradation activity, and approximately 99% degradation of MB was achieved at pH 10. This is possibly because the higher pH value leads to the formation of negative charges on the surface. Since MB is a cationic dye that possesses a positive charge and the dyes are adsorbed on the surface, which possess higher amounts of OH• radical ions, hence the MB undergoes removal by a dual phenomenon, i.e., adsorption/photodegradation, that leads to better removal of MB from the system. However, in the case of MY, an anionic dye, the enhanced degradation at higher pH can be attributed to higher amounts of OH• radical ions generated by the photocatalyst, due to which the photodegradation process is performed more efficiently at higher pH values [51,52].
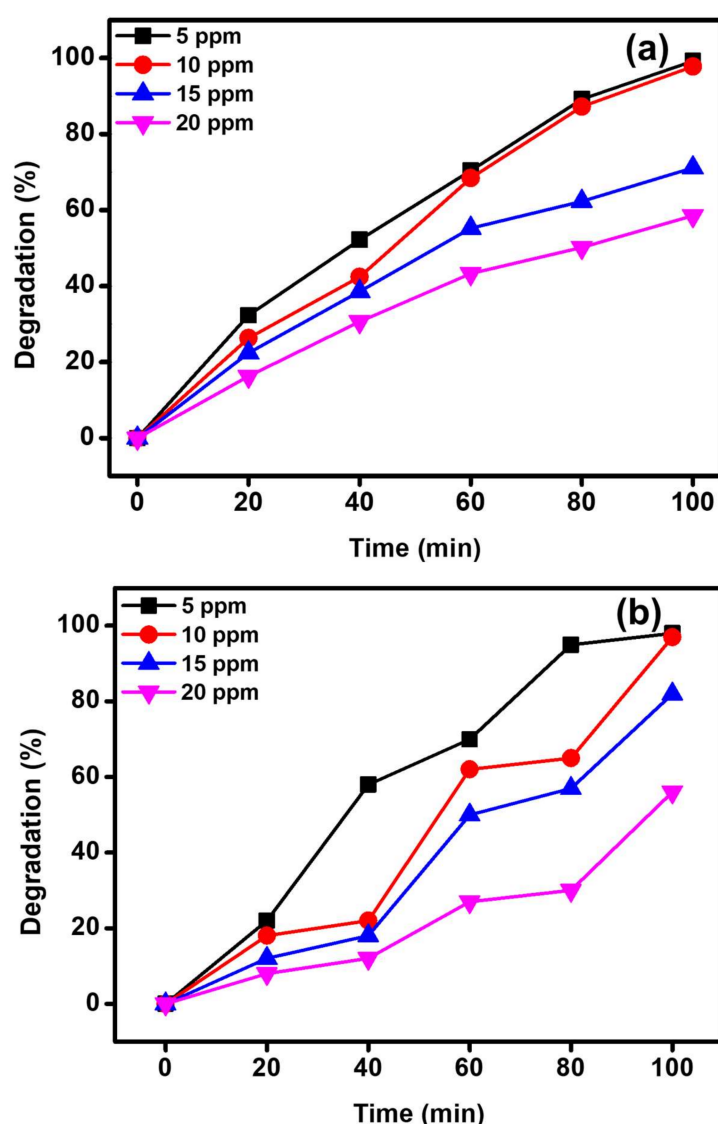

Figure 9. Impact of (**a**) MB and (**b**) MY concentration on the catalytic performance of the ZnO photocatalyst.
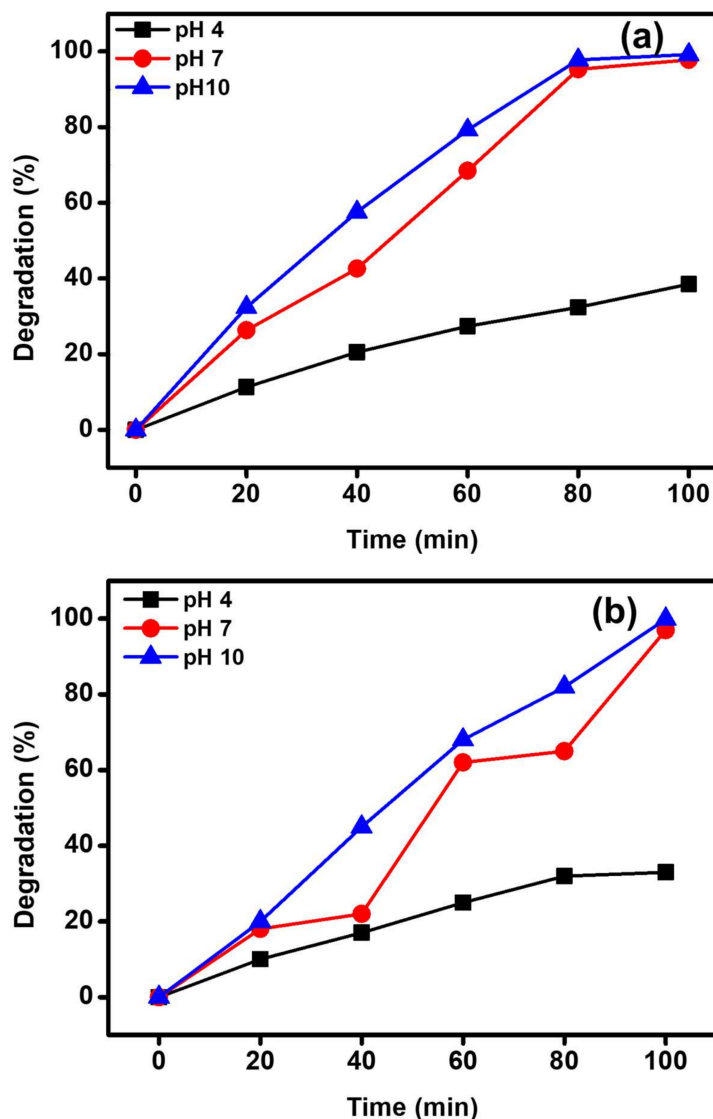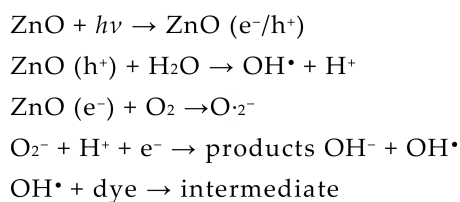
Figure 10. Impact of pH value on the catalytic performance of the ZnO photocatalyst on the (**a**) MB and (**b**) MY photodegradation.

The possible reaction mechanism of ZnO is shown in Figure 11a. When the photons are illuminated on the surface of the nanocrystals, the valance band (VB) electrons become excited and travel to the conduction band (CB). In this way, the formed conduction band electrons and valance band holes initiate the reduction and oxidation reactions, respectively. The superoxide radicals produced by the reduction reaction combine with hydroxyl radicals and generate the H_2O_2, which further produces the $OH^\bullet$ radicals. The produced hydroxyl radicals can degrade the dye molecule.

The probable reaction mechanism for the MB dye degradation process is presented in Scheme 1.

ZnO + $h\nu$ → ZnO (e⁻/h⁺)

ZnO (h⁺) + H_2O → $OH^\bullet$ + H⁺

ZnO (e⁻) + O_2 → $O^{\cdot 2-}$

O_2^- + H⁺ + e⁻ → products OH⁻ + $OH^\bullet$

$OH^\bullet$ + dye → intermediate
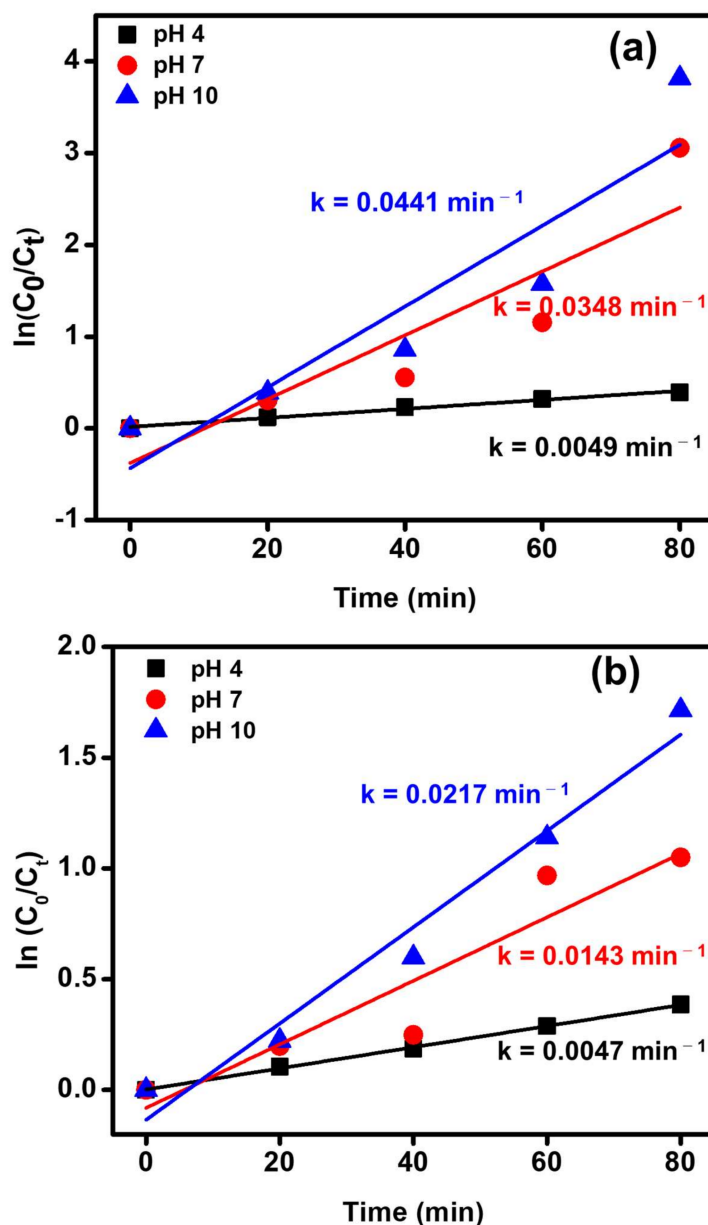
Scheme 1. Possible reaction mechanism.

Figure 11. Pseudo-first-order kinetics for (**a**) MB and (**b**) MY photodegradation over the ZnO photocatalyst.

Figure 11a,b illustrates the photocatalytic decomposition of MB and MY dyes using the ZnO photocatalyst for various pH values at optimum reaction circumstances, followed by a pseudo-first-order reaction kinetics, which is given by Equation (3) as:

$$\ln(C_0/C_t) = \text{k}t \tag{3}$$

where C_0 and C_t are the initial dye concentration and final dye concentration at time t, correspondingly, and k is the first-order rate constant. The obtained degradation rate constants (k) are 0.0049, 0.0348 and 0.0441 min^{-1} for MB dye and 0.0047, 0.0143 and 0.0217 min^{-1} for MY dye at the pH values of 4, 7 and 10, respectively.

A comparison of the outstanding photocatalytic degradation efficacy of the ZnO photocatalyst for the photodecomposition of different dyes with formerly reported ZnO-based photosystems is compiled in Table 1. It was distinctly noticed that the ZnO photocatalyst in the current study exhibited superior photodegradation efficiency compared to the previously reported catalysts.

Table 1. Comparative data of photocatalytic degradation of organic dyes using ZnO nanoparticle-based photocatalysts.

Catalyst	Dye		Light Source	Catalyst Amount	Time (min)	Degradation (%)	Ref.
	Name	Concentration					
ZnO NCs		5 ppm	UV irradiation	15 mg	100	99	Herein
ZnO		15 ppm	Hg lamp 10 W	100 mg	120	90	[53]
ZnO NCs		10 ppm	UV irradiation	200 mg	160	95	[26]
Au-ZnO		10 ppm	UV irradiation	30 mg	180	95	[54]
ZnO/GO		5 ppm	Mercury vapor lamp	80 mg	240	99	[55]
ZnO/GdCoO$_3$	Methylene Blue	6 ppm	Visible light	3 mg	120	92.4	[56]
ZnO-SnO$_2$ nano-cubes		10 ppm	UV irradiation	NA	60	97.2	[57]
ZnO nanorod		10 ppm	Sunlight	NA	150	100	[58]
Ag-ZnO-Graphene		0.05 mM	UV irradiation	NA	360	96	[59]
GP-ZnO-NCs		10 ppm	UV irradiation	NA	180	89	[60]
Fe-Co-ZnO		5 ppm	Sunlight	30 mg	60	98.8	[61]
ZnO/ZnSe/MoSe$_2$		30 ppm	Visible light	30 mg	180	91.5	[62]
ZnO NCs		5 ppm	UV irradiation	15 mg	100	97	Herein
Sm-g-C$_3$N$_4$-550-4 h		20 mM	Visible light	100 mg	360	83.7	[63]
ZnO		50 ppm	UV irradiation	1 g	180	97	[64]
TiO$_2$-coupled to membrane		30 ppm	UV irradiation	500 mg	300	43	[65]
CdO-Al$_2$O$_3$	Metanil yellow	25 mM	Visible light	6 mg	75	82	[66]
N-TiO$_2$		0.018 mM	Visible light	500 mg	360	89	[67]
PVA/AA-TiO$_2$		0.88 mM	UV irradiation	500 mg	110	90	[68]
SnS$_2$-ZnS		0.025 mM	Visible light	6 mg	180	90	[69]
Anatase TiO$_2$		6 ppm	UV irradiation	100 mg	90	81	[70]
CP1-CP4		0.01 mM	Visible light + H$_2$O$_2$	15 mg	180	83	[71]

4. Conclusions

In this study, we reported on the successful green synthesis of ZnO nanocrystals using coconut husk extract. The characterization of the as-prepared material revealed the crystalline nature and nano-sized ZnO. The FT-IR spectra revealed the presence of a Zn(OH)$_2$ impurity along with ZnO, while the other characterization techniques, such as XRD and Raman spectroscopy, did not reveal its presence, indicating the presence of Zn(OH)$_2$ in only trace amounts. The as-prepared material was tested as a photocatalyst for the degradation of methylene blue dye, a harmful industrial effluent. The photocatalyst displayed excellent degradation efficiency under UV light, with ~99% degradation in 100 min. It was also revealed that the photocatalyst can be optimally used for MB dye degradation in the concentration range between 5 and 10 ppm and that pH 7 and pH 10 are optimum for the best catalytic activity. The kinetics of the catalyst revealed that the degradation follows a pseudo-first-order reaction kinetics.

their constant support and the Technical Research Centre—Microscopy lab at JNCASR for providing microscopy facilities.

References

1. Selim, Y.A.; Azb, M.A.; Ragab, I.; Abd El-Azim, M.H.M. Green synthesis of Zinc oxide nanoparticles using Aqueous extract of *Deverra tortuosa* and their Cytotoxic activities. *Sci. Rep.* **2020**, *10*, 3445. [CrossRef]
2. Syed, M.A. Advances in nanodiagnostic techniques for microbial agents. *Biosens. Bioelectron.* **2014**, *51*, 391–400. [CrossRef]
3. Chen, G.; Roy, I.; Yang, C.; Prasad, P.N. Nanochemistry and nanomedicine for nanoparticle-based diagnostics and therapy. *Chem. Rev.* **2016**, *116*, 2826–2885. [CrossRef]
4. Sirelkhatim, A.; Mahmud, S.; Seeni, A.; Kaus, N.H.M.; Ann, L.C.; Bakhori, S.K.M.; Hasan, H.; Mohamad, D. Review on Zinc Oxide nanoparticles: Antibacterial activity and toxicity mechanism. *Nano-Micro Lett.* **2015**, *7*, 219–242. [CrossRef]
5. Adil, S.F.; Assal, M.E.; Shaik, M.R.; Kuniyil, M.; Hashmi, A.; Khan, M.; Khan, A.; Tahir, M.N.; Al-Warthan, A.; Siddiqui, M.R.H. Efficient aerial oxidation of different types of alcohols using ZnO nanoparticle–MnCO$_3$—graphene oxide composites. *Appl. Organomet. Chem.* **2020**, *34*, e5718. [CrossRef]
6. Assal, M.E.; Shaik, M.R.; Kuniyil, M.; Khan, M.; Al-Warthan, A.; Alharthi, A.I.; Varala, R.; Siddiqui, M.R.H.; Adil, S.F. Ag$_2$O nanoparticles/MnCO$_3$–MnO$_2$ or–Mn$_2$O$_3$/highly reduced graphene oxide composites as an efficient and recyclable oxidation catalyst. *Arab. J. Chem.* **2019**, *12*, 54–68. [CrossRef]
7. Diallo, A.; Mothudi, B.M.; Manikandan, E.; Maaza, M. Luminescent Eu$_2$O$_3$nanocrystals by *Aspalathus linearis'* extract: Structural and optical properties. *J. Nanophotonics* **2016**, *10*, 026010. [CrossRef]
8. Eslami, A.; Amini, M.M.; Yazdanbakhsh, A.R.; Mohseni-Bandpei, A.; Safari, A.A.; Asadi, A. N, S co-doped TiO$_2$ nanoparticles and nanosheets in simulated solar light for photocatalytic degradation of non-steroidal anti-inflammatory drugs in water: A comparative study. *J. Chem. Technol. Biotechnol.* **2016**, *91*, 2693–2704. [CrossRef]
9. Fujita, Y.; Yanase, S.; Nishikori, H.; Hiragino, Y.; Furubayashi, Y.; Lin, J.; Yoshida, T. Near ultraviolet light emitting diodes using ZnMgO: N/ZnO hetero-junction grown by MOVPE. *J. Cryst. Growth* **2017**, *464*, 226–230. [CrossRef]
10. Park, C.; Lee, J.; So, H.-M.; Chang, W.S. An ultrafast response grating structural ZnO photodetector with back-to-back Schottky barriers produced by hydrothermal growth. *J. Mater. Chem. C* **2015**, *3*, 2737–2743. [CrossRef]
11. Nicolaev, A.; Mitran, T.; Iftimie, S.; Nemnes, G. Optimization of halide perovskite solar cells based on nanocolumnar ZnO. *Sol. Energy Mater. Sol. Cells* **2016**, *158*, 202–208. [CrossRef]
12. Ohashi, H.; Hagiwara, M.; Fujihara, S. Solvent-assisted microstructural evolution and enhanced performance of porous ZnO films for plastic dye-sensitized solar cells. *J. Power Sources* **2017**, *342*, 148–156. [CrossRef]
13. Di Mauro, A.; Cantarella, M.; Nicotra, G.; Privitera, V.; Impellizzeri, G. Low temperature atomic layer deposition of ZnO: Applications in photocatalysis. *Appl. Catal. B Environ.* **2016**, *196*, 68–76. [CrossRef]
14. Könenkamp, R.; Dloczik, L.; Ernst, K.; Olesch, C. Nano-structures for solar cells with extremely thin absorbers. *Phys. E Low-Dimens. Syst. Nanostructures* **2002**, *14*, 219–223. [CrossRef]
15. Al-Ghamdi, A.A.; Al-Hartomy, O.A.; El Okr, M.; Nawar, A.; El-Gazzar, S.; El-Tantawy, F.; Yakuphanoglu, F. Semiconducting properties of Al doped ZnO thin films. *Spectrochim. Acta Part A Mol. Biomol. Spectrosc.* **2014**, *131*, 512–517. [CrossRef]
16. Tahir, M.N. Non-aqueous synthesis of AuCu@ZnO alloy-semiconductor heteroparticles for photocatalytical degradation of organic dyes. *J. Saudi Chem. Soc.* **2021**, *25*, 101210. [CrossRef]
17. Yang, J.L.; An, S.J.; Park, W.I.; Yi, G.-C.; Choi, W. Photocatalysis using ZnO thin films and nanoneedles grown by metal-organic chemical vapor deposition. *Adv. Mater.* **2004**, *16*, 1661–1664. [CrossRef]
18. Webster, T.J.; Seil, J.T. Antimicrobial applications of nanotechnology: Methods and literature. *Int. J. Nanomed.* **2012**, *7*, 2767–2781. [CrossRef]
19. Kumar, R.; Umar, A.; Kumar, G.; Nalwa, H.S. Antimicrobial properties of ZnO nanomaterials: A review. *Ceram. Int.* **2017**, *43*, 3940–3961. [CrossRef]
20. Jones, N.; Ray, B.; Ranjit, K.T.; Manna, A.C. Antibacterial activity of ZnO nanoparticle suspensions on a broad spectrum of microorganisms. *FEMS Microbiol. Lett.* **2008**, *279*, 71–76. [CrossRef]
21. Sangeetha, G.; Rajeshwari, S.; Venckatesh, R. Green synthesis of zinc oxide nanoparticles by aloe barbadensis miller leaf extract: Structure and optical properties. *Mater. Res. Bull.* **2011**, *46*, 2560–2566. [CrossRef]
22. Yang, S.J.; Park, C.R. Facile preparation of monodisperse ZnO quantum dots with high quality photoluminescence characteristics. *Nanotechnology* **2007**, *19*, 035609. [CrossRef] [PubMed]
23. Habibi, M.H.; Rahmati, M.H. The effect of operational parameters on the photocatalytic degradation of Congo red organic dye using ZnO–CdS core–shell nano-structure coated on glass by Doctor Blade method. *Spectrochim. Acta Part A Mol. Biomol. Spectrosc.* **2015**, *137*, 160–164. [CrossRef] [PubMed]
24. Water, W.; Chu, S.-Y.; Juang, Y.-D.; Wu, S.-J. Li$_2$CO$_3$-doped ZnO films prepared by RF magnetron sputtering technique for acoustic device application. *Mater. Lett.* **2002**, *57*, 998–1003. [CrossRef]
25. Li, M.; Bala, H.; Lv, X.; Ma, X.; Sun, F.; Tang, L.; Wang, Z. Direct synthesis of monodispersed ZnO nanoparticles in an aqueous solution. *Mater. Lett.* **2007**, *61*, 690–693. [CrossRef]

26. Dodoo-Arhin, D.; Asiedu, T.; Agyei-Tuffour, B.; Nyankson, E.; Obada, D.; Mwabora, J. Photocatalytic degradation of Rhodamine dyes using zinc oxide nanoparticles. *Mater. Today Proc.* **2020**, *38*, 809–815. [CrossRef]

27. Alanazi, H.S.; Ahmad, N.; Alharthi, F.A. Synthesis of Gd/N co-doped ZnO for enhanced UV-vis and direct solar-light-driven photocatalytic degradation. *RSC Adv.* **2021**, *11*, 10194–10202. [CrossRef]

28. Wang, L.; Muhammed, M. Synthesis of zinc oxide nanoparticles with controlled morphology. *J. Mater. Chem.* **1999**, *9*, 2871–2878. [CrossRef]

29. Bahnemann, D.W.; Kormann, C.; Hoffmann, M.R. Preparation and characterization of quantum size zinc oxide: A detailed spectroscopic study. *J. Phys. Chem.* **1987**, *91*, 3789–3798. [CrossRef]

30. Zhang, J.; Sun, L.D. Control of ZnO morphology via a simple solution route. *Chem. Mater.* **2002**, *14*, 4172–4177. [CrossRef]

31. Chen, W.; Caia, W.; Zhangb, L.; Wanga, G.; Zhanga, L. Sonochemical processes and formation of gold nanoparticles within pores of mesoporous silica. *J. Colloid Interface Sci.* **2001**, *238*, 291–295. [CrossRef]

32. Wojnarowicz, J.; Chudoba, T.; Lojkowski, W. A review of microwave synthesis of Zinc oxide nanomaterials: Reactants, process parameters and morphologies. *Nanomaterials* **2020**, *10*, 1086. [CrossRef]

33. Sobha, K.; Surendranath, K.; Meena, V.; Jwala, T.K.; Swetha, N.; Latha, K. Emerging trends in nanobiotechnology. *Biotechnol. Mol. Biol. Rev.* **2010**, *4*, 1–12.

34. Mydeen, S.S.; Kumar, R.R.; Kottaisamy, M.; Vasantha, V. Biosynthesis of ZnO nanoparticles through extract from Prosopis juliflora plant leaf: Antibacterial activities and a new approach by rust-induced photocatalysis. *J. Saudi Chem. Soc.* **2020**, *24*, 393–406. [CrossRef]

35. Wang, W.; Huang, G. Characterisation and utilization of natural coconut fibres composites. *Mater. Des.* **2009**, *30*, 2741–2744. [CrossRef]

36. Esquenazi, D.; Wigg, M.D.; Miranda, M.M.; Rodrigues, H.M.; Tostes, J.B.; Rozental, S.; da Silva, A.J.; Alviano, C.S. Antimicrobial and antiviral activities of polyphenolics from *Cocos nucifera Linn.* (*Palmae*) husk fiber extract. *Res. Microbiol.* **2002**, *153*, 647–652. [CrossRef]

37. Buamard, N.; Benjakul, S. Ethanolic coconut husk extract: In vitro antioxidative activity and effect on oxidative stability of shrimp oil emulsion. *Eur. J. Lipid Sci. Technol.* **2017**, *119*, 1700131. [CrossRef]

38. Akinyele, T.A.; Okoh, O.O.; Akinpelu, D.A.; Okoh, A.I. In-vitro antibacterial properties of crude aqueous and n-Hexane extracts of the husk of *Cocos Nucifera*. *Molecules* **2011**, *16*, 2135–2145. [CrossRef] [PubMed]

39. Agarwal, M.B.; Malaidurai, M.; Sahoo, S.; Thangavel, R. Fabrication and characterization of Mn doped ZnO nanoarrays prepared by two step process. In Proceedings of the Third International Conference on Material Science, Smart Structures and Applications, Erode, India, 15–16 October 2020; Volume 2327, p. 020010.

40. Kumar, P.; Singh, J.; Parashar, V.; Singh, K.; Tiwari, R.S.; Srivastava, O.N.; Ramam, K.; Pandey, A.C. Investigations on structural, optical and second harmonic generation in solvothermally synthesized pure and Cr-doped ZnO nanoparticles. *CrystEngComm* **2012**, *14*, 1653–1658. [CrossRef]

41. Kleinwechter, H.; Janzen, C.; Knipping, J.; Wiggers, H.; Roth, P. Formation and properties of ZnO nano-particles from gas phase synthesis processes. *J. Mater. Sci.* **2002**, *37*, 4349–4360. [CrossRef]

42. Das, J.; Khushalani, D. Nonhydrolytic route for synthesis of ZnO and its use as a recyclable photocatalyst. *J. Phys. Chem. C* **2010**, *114*, 2544–2550. [CrossRef]

43. Momot, A.; Amini, M.N.; Reekmans, G.; Lamoen, D.; Partoens, B.; Slocombe, D.R.; Elen, K.; Adriaensens, P.; Hardy, A.; Van Bael, M.K. A novel explanation for the increased conductivity in annealed Al-doped ZnO: An insight into migration of aluminum and displacement of zinc. *Phys. Chem. Chem. Phys.* **2017**, *19*, 27866–27877. [CrossRef] [PubMed]

44. Russo, V.; Ghidelli, M.; Gondoni, P.; Casari, C.S.; Bassi, A.L. Multi-wavelength Raman scattering of nanostructured Al-doped zinc oxide. *J. Appl. Phys.* **2014**, *115*, 073508. [CrossRef]

45. Georgekutty, R.; Seery, M.; Pillai, S.C. A highly efficient Ag-ZnO photocatalyst: Synthesis, properties, and mechanism. *J. Phys. Chem. C* **2008**, *112*, 13563–13570. [CrossRef]

46. Montenegro, D.N.; Hortelano, V.; Martínez, O.; Martinez-Tomas, M.C.; Sallet, V.; Muñoz-Sanjose, V.; Jiménez, J. Non-radiative recombination centres in catalyst-free ZnO nanorods grown by atmospheric-metal organic chemical vapour deposition. *J. Phys. D Appl. Phys.* **2013**, *46*, 235302. [CrossRef]

47. Lin, M.; Ye, E.; Zhang, J. 3D TEM study on hollow α-Fe$_2$O$_3$ nanostructures and nanorings. *Prog. Nat. Sci.* **2019**, *29*, 685–689. [CrossRef]

48. Ogunyemi, S.O.; Abdallah, Y.; Zhang, M.; Fouad, H.; Hong, X.; Ibrahim, E.; Masum, M.I.; Hossain, A.; Mo, J.; Li, B. Green synthesis of zinc oxide nanoparticles using different plant extracts and their antibacterial activity against *Xanthomonas oryzae* pv. oryzae. *Artif. Cells Nanomed. Biotechnol.* **2019**, *47*, 341–352. [CrossRef]

49. Zhang, Z.; Ma, Y.; Bu, X.; Wu, Q.; Hang, Z.; Dong, Z.; Wu, X. Facile one-step synthesis of TiO$_2$/Ag/SnO$_2$ ternary heterostructures with enhanced visible light photocatalytic activity. *Sci. Rep.* **2018**, *8*, 1–11.

50. Nezam, A.; Saffar-Teluri, A.; Hassanzadeh-Tabrizi, S. The high efficiency of Al$_2$O$_3$-SiO$_2$-CuO nanocomposites as an adsorbent: Synthesis and dye removal efficiency. *Res. Chem. Intermed.* **2016**, *42*, 4999–5011. [CrossRef]

51. Motlagh, M.M.; Hassanzadeh-Tabrizi, S.; Saffar-Teluri, A. Sol–gel synthesis of Mn$_2$O$_3$/Al$_2$O$_3$/SiO$_2$ hybrid nanocomposite and application for removal of organic dye. *J. Sol-Gel Sci. Technol.* **2015**, *73*, 9–13. [CrossRef]

52. Rahmi, R.; Lubis, S.; Az-Zahra, N.; Puspita, K.; Iqhrammullah, M. Synergetic photocatalytic and adsorptive removals of metanil yellow using TiO$_2$/grass-derived cellulose/chitosan (TiO$_2$/GC/CH) film composite. *Int. J. Eng.* **2021**, *34*, 1827–1836.

53. Soto-Robles, C.; Nava, O.; Cornejo, L.; Lugo, E.; Vilchis-Nestor, A.; Castro-Beltrán, A.; Luque, P. Biosynthesis, characterization and photocatalytic activity of ZnO nanoparticles using extracts of *Justicia spicigera* for the degradation of methylene blue. *J. Mol. Struct.* **2021**, *1225*, 129101. [CrossRef]

54. Ahmad, M.; Rehman, W.; Khan, M.M.; Qureshi, M.T.; Gul, A.; Haq, S.; Ullah, R.; Rab, A.; Menaa, F. Phytogenic fabrication of ZnO and gold decorated ZnO nanoparticles for photocatalytic degradation of Rhodamine B. *J. Environ. Chem. Eng.* **2021**, *9*, 104725. [CrossRef]

55. Puneetha, J.; Kottam, N.; Rathna, A. Investigation of photocatalytic degradation of crystal violet and its correlation with bandgap in ZnO and ZnO/GO nanohybrid. *Inorg. Chem. Commun.* **2021**, *125*, 108460. [CrossRef]

56. Yulizar, Y.; Eprasatya, A.; Apriandanu, D.O.B.; Yunarti, R.T. Facile synthesis of ZnO/GdCoO$_3$ nanocomposites, characterization and their photocatalytic activity under visible light illumination. *Vacuum* **2021**, *183*, 109821. [CrossRef]

57. Kumar, R.; Umar, A.; Chauhan, M.; Al-Hadeethi, Y. ZnO-SnO$_2$ nanocubes for fluorescence sensing and dye degradation applications. *Ceram. Int.* **2021**, *47*, 6201–6210. [CrossRef]

58. Biswal, H.J.; Yadav, A.; Vundavilli, P.R.; Gupta, A. High aspect ZnO nanorod growth over electrodeposited tubes for photocatalytic degradation of EtBr dye. *RSC Adv.* **2021**, *11*, 1623–1634. [CrossRef]

59. Beura, R.; Pachaiappan, R.; Paramasivam, T. Photocatalytic degradation studies of organic dyes over novel Ag-loaded ZnO-graphene hybrid nanocomposites. *J. Phys. Chem. Solids* **2021**, *148*, 109689. [CrossRef]

60. Park, J.K.; Rupa, E.J.; Arif, M.H.; Li, J.F.; Anandapadmanaban, G.; Kang, J.P.; Kim, M.; Ahn, J.C.; Akter, R.; Yang, D.C.; et al. Synthesis of zinc oxide nanoparticles from *Gynostemma pentaphyllum* extracts and assessment of photocatalytic properties through malachite green dye decolorization under UV illumination-A Green Approach. *Optik* **2021**, *239*, 166249. [CrossRef]

61. Nadeem, M.S.; Munawar, T.; Mukhtar, F.; Rahman, M.N.U.; Riaz, M.; Iqbal, F. Enhancement in the photocatalytic and antimicrobial properties of ZnO nanoparticles by structural variations and energy bandgap tuning through Fe and Co co-doping. *Ceram. Int.* **2021**, *47*, 11109–11121. [CrossRef]

62. Yang, Y.; Wu, Z.; Yang, R.; Li, Y.; Liu, X.; Zhang, L.; Yu, B. Insights into the mechanism of enhanced photocatalytic dye degradation and antibacterial activity over ternary ZnO/ZnSe/MoSe$_2$ photocatalysts under visible light irradiation. *Appl. Surf. Sci.* **2021**, *539*, 148220. [CrossRef]

63. Masunga, N.; Mamba, B.B.; Kefeni, K.K. Trace samarium doped graphitic carbon nitride photocatalytic activity toward metanil yellow dye degradation under visible light irradiation. *Colloids Surf. A Physicochem. Eng. Asp.* **2020**, *602*, 125107. [CrossRef]

64. Khezrianjoo, S.; Revanasiddappa, H.D. Photocatalytic degradation of acid yellow 36 using Zinc oxide photocatalyst in aqueous media. *J. Catal.* **2013**, *2013*, 1–6. [CrossRef]

65. Mozia, S.; Morawski, A.W.; Toyoda, M.; Tsumura, T. Effect of process parameters on photodegradation of Acid Yellow 36 in a hybrid photocatalysis–membrane distillation system. *Chem. Eng. J.* **2009**, *150*, 152–159. [CrossRef]

66. Balamurugan, S.; Balu, A.; Srivind, J.; Usharani, K.; Narasimman, V.; Suganya, M.; Nagarethinam, V. CdO Al$_2$O$_3$—A composite material with enhanced photocatalytic activity against the degradation of MY dye. *Vacuum* **2019**, *159*, 9–16. [CrossRef]

67. Chakrabortty, D.; Gupta, S.S. Decolourisation of Metanil Yellow by visible-light photocatalysis with N-doped TiO$_2$ nanoparticles: Influence of system parameters and kinetic study. *DESALINATION Water Treat.* **2013**, *52*, 5528–5540. [CrossRef]

68. El-Rehim, H.A.A.; Hegazy, E.-S.A.; Diaa, D.A. Photo-catalytic degradation of Metanil Yellow dye using TiO$_2$ immobilized into polyvinyl alcohol/acrylic acid microgels prepared by ionizing radiation. *React. Funct. Polym.* **2012**, *72*, 823–831. [CrossRef]

69. Prabha, D.; Usharani, K.; Ilangovan, S.; Narasimman, V.; Balamurugan, S.; Suganya, M.; Srivind, J.; Nagarethinam, V.S.; Balu, A.R. Thermal behavior and comparative study on the visible light driven photocatalytic performance of SnS$_2$–ZnS nanocomposite against the degradation of anionic and cationic dyes. *J. Mater. Sci. Mater. Electron.* **2018**, *29*, 18708–18717. [CrossRef]

70. Safni, S.; Sari, F.; Maizatisna, M.; Zulfarman, Z. Degradation of metanil yellow dye using sonolysis and photolysis methods with addition of anatase TiO$_2$. *Indones. J. Mater. Sci.* **2009**, *11*, 47–51.

71. Bisht, K.; Rachuri, Y.; Parmar, B.; Suresh, E. Mixed ligand coordination polymers with flexible bis-imidazole linker and angular sulfonyldibenzoate: Crystal structure, photoluminescence and photocatalytic activity. *J. Solid State Chem.* **2014**, *213*, 43–51. [CrossRef]